Computers & Geosciences 100 (2017) 10–26

Contents lists available at ScienceDirect

Computers & Geosciences

journal homepage: www.elsevier.com/locate/cageo

Research paper

Benchmarking Defmod, an open source FEM code for modeling episodic fault rupture

Chunfang Meng

Earth Resources Laboratory, Massachusetts Institute of Technology, Cambridge, MA, USA

ARTICLE INFO

Keywords:
Induced earthquake
Finite element
Fault
Poroelasticity
Dynamic rupture
Defmod

ABSTRACT

We present Defmod, an open source (linear) finite element code that enables us to efficiently model the crustal deformation due to (quasi-)static and dynamic loadings, poroelastic flow, viscoelastic flow and frictional fault slip. Ali (2015) provides the original code introducing an implicit solver for (quasi-)static problem, and an explicit solver for dynamic problem. The fault constraint is implemented via Lagrange Multiplier. Meng (2015) combines these two solvers into a hybrid solver that uses failure criteria and friction laws to adaptively switch between the (quasi-)static state and dynamic state. The code is capable of modeling episodic fault rupture driven by quasi-static loadings, e.g. due to reservoir fluid withdraw or injection. Here, we focus on benchmarking the Defmod results against some establish results.

1. Quasi-static crustal deformation

When a region is subjected to a gradual loading process, such as tectonic stress changes, viscoelastic relaxation, and pore pressure changes, it deforms in a quasi-static manner. Every snapshot of a quasi-static process, as opposed to a dynamic process, satisfies stress equilibrium. The inertial force is considered negligible, since the net force is small, and the time scale is large.

For linear constitutive law and small strain problems, the finite element method, Zienkiewicz (2000), provides a system of linear equations describing the (quasi-)static state. Eq. (1) lists the absolute and incremental versions of the linear equation, Smith and Griffiths, 2004.

$$\mathbf{K}_n\mathbf{U}_n = \mathbf{F}_n, \text{ absolute, } \mathbf{K}_n\Delta\mathbf{U}_n = \Delta\mathbf{F}_n, \text{ incremental.} \tag{1}$$

where, $\mathbf{K}$ is the system stiffness matrix, $\mathbf{U}$ is the solution vector and $\mathbf{F}$ is the nodal force, including fluid source. The subscript n is the time index. In this study, we use the incremental equation. The solution space $\Delta\mathbf{U}_n$ of a poroelastic problem contains the nodal displacement and pressure, $\Delta\mathbf{U}_n = \begin{bmatrix}\Delta\mathbf{u}_n \\ \Delta\mathbf{p}_n\end{bmatrix}$, whereas the solution for an elastic problem is only the nodal displacement.

The stiffness matrix $\mathbf{K_n}$ and RHS function $\Delta\mathbf{F}_n$ are also different for the elastic and poroelastic problems, Eq. (2).

$$(\mathbf{K}_n,\ \Delta\mathbf{F}_n) = \begin{cases} (\mathbf{K}_e,\ \Delta\mathbf{f}_n) & \text{, elastic.} \\ \left(\begin{bmatrix}\mathbf{K}_e & \mathbf{H} \\ -\mathbf{H}^T & \Delta t\mathbf{K}_c + \mathbf{S}_p\end{bmatrix}, \begin{bmatrix}\Delta\mathbf{f}_n \\ \mathbf{q}_n - \Delta t\mathbf{K}_c\mathbf{p}_{n-1}\end{bmatrix}\right) & \text{, poroelastic.} \end{cases} \tag{2}$$

where, $\mathbf{K}_e$ is the elastic stiffness matrix, depending on the elastic constants of the solid. $\mathbf{K}_c$ is the fluid stiffness matrix, depending on the fluid flow conductivity. $\mathbf{H}$ is the coupling matrix, depending on the Biot's coefficient. $\mathbf{S}_p$ is the storage matrix, depending the solid compressibility and porosity, and the fluid compressibility. Smith and Griffiths (2004) provide the detailed formulation for these matrices and vectors. Note, the stiffness matrix $\mathbf{K}_n$ is constant for evenly spaced time step Δt. In a later section, we show that for Newtonian viscoelasticity, $\mathbf{K}_n$ is, although modified, still independent of time. $\mathbf{f}_n$ and $\mathbf{q}_n$ are nodal force and fluid source respectively. The detailed formulations of these matrices and RHS vectors are given in Appendix A

2. Poroelastic model and benchmark

Unstable pressure is caused by using linear elements, known as the Ladyzenskaja-Babuska-Brezzi restrictions. The local pressure projection scheme, Bochev and Dohrmann (2006), is implemented to stabilize the pore pressure,

$$\mathbf{F}_{n+1} = \mathbf{F}_{n+1} - \begin{bmatrix}\mathbf{0} \\ \mathbf{H}_s\mathbf{p}_n\end{bmatrix},\ \mathbf{K}_{n+1} = \mathbf{K}_{n+1} + \begin{bmatrix}\mathbf{0} & \mathbf{0} \\ \mathbf{0} & \mathbf{H}_s\end{bmatrix}, \text{ where}$$
$$, \mathbf{H}_s = \int_\Omega (\mathbf{N} - (1/n_e)I_{\mathbf{N}})^{\mathrm{T}}(\mathbf{N} - (1/n_e)I_{\mathbf{N}})/(2G)\,d\Omega, \tag{3}$$

E-mail address: cmeng@mit.edu.

http://dx.doi.org/10.1016/j.cageo.2016.11.014
Received 7 July 2016; Received in revised form 27 November 2016; Accepted 29 November 2016
Available online 02 December 2016

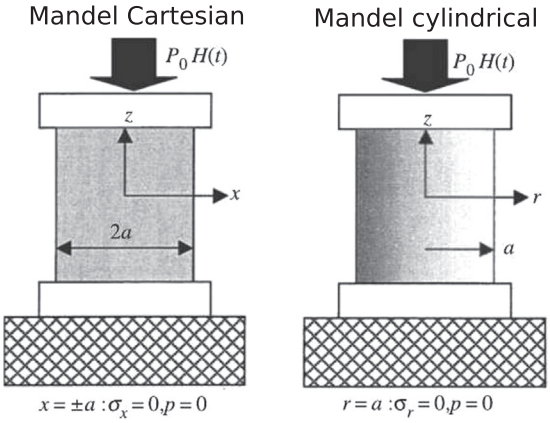

Fig. 1. Schematics of the Mandel benchmark problem by Kurashige et al. (2005).

N is the shape function of an element e, n_e is the node count of the element, and G is the shear modulus.

To benchmark the poroelastic model, we compare the Defmod results against the well known Mandel solution. Fig. 1 illustrates the Mandel problem.

At time t=0, the boundaries at $r = \pm a$ of a homogeneously pressurized poroelastic matrix suddenly has the pressure dropped from p_0 to zero. And, a compressional loading $\sigma_z = p_0$ is placed on a rigid plate at the matrix top. The pore fluid will then flow towards the side boundaries accompanied by matrix deformation. Because the matrix is axially symmetric with rigid top and bottom, the pressure, deformation and stress only vary in r and time, not in z. These values have closed forms in the Laplace frequency domain, Kurashige et al. (2005). Here, we apply numerical inverse Laplace transform, Talbot's method, to have the semi analytical pressure in the time domain.

There are two difficulties to simulate the Mandel problem with a quasi-static model. First, the initial pressure imposed by the Mandel problem results a singular pressure gradient at the side boundaries. Second, implementation of the rigid loading plate requires solving a contact problem. Thanks for the pressure stabilization method as mentioned, the models only show some spatial oscillation near the side boundaries at time zero. The rigid loading plate can be replaced by uniform loading to avoid the contact problem. This requires the matrix aspect ratio height /a to be large enough such that the bottom, at z=0, will not *feel* the tilted deformation at the top.

The poroelastic model parameters are listed in Table 1

Fig. 2 plots the initial pressure of a 2D and a 3D poroelastic models approximating the Cartesian and cylindrical Mandel problems respectively. Because of the symmetry, we only need to consider half of the Cartesian domain and a quarter of the cylindrical domain in Fig. 1.

The numerical pressure should be normalized by p_0 to be comparable with the Mandel pressure, Kurashige et al. (2005). A quasi-static model always produces solutions of some stress equilibrium states. Therefore, the model, being continuum, cannot produce the theoretical initial pressure which has a sharp pressure drop, infinite gradient, at x=a. To resolve this, we sync the model pressure, at r=0, z=0, $t = t_1$, $p_{\text{model}}(0, 0, t_1)$ with the Mandel pressure, at r =0, $t = t_1$, $p_{\text{Mandel}}(0, t_1)$, i.e. multiply all the model pressures by $\frac{p_{\text{Mandel}}(0,t_1)}{p_{\text{model}}(0,0,t_1)}$, t_1 being the first/smallest nonzero model time.

Fig. 3 plots the normalized pressure as a function of r/a by the 2D and 3D models, at z=0, against the Cartesian and cylindrical Mandel solutions respectively. Where the normalized time τ_t is given by $\tau_t = \frac{tK}{Sa^2}$, K being the solid bulk modulus and S being the storage coefficient. Because of the difference between the model and Mandel problem in the initial state as mentioned, the comparisons show greater discrepancy at $\tau_t = 0$ than at later times.

Note that, the initial state is not only missed by the numerical solution but also missed by the analytical solution, using the inverse Laplace transform, Kurashige et al. (2005). We put the time zero pressure there just for reference. Since the analytical solution is dimensionless, we have to normalize the numerical pressure in order have a comparison, similar to Jha and Juanes (2014).

Fig. 4 plots the normalized pressure as a function of time at $(r) = 0$ by the 2D and 3D models, at z=0, against the Cartesian and cylindrical Mandel solutions respectively due to dimensional effect.

The 2D (Cartesian) and 3D (cylindrical) models (Mendel solutions) show significantly different pressure curves.

To demonstrate the relation between the mesh resolution and the results, especially the pressure peak at t=0 and near r=a, we make two meshes for the same 3D model. One of them has 10 cells along the radius, and another one has 20 cells along the radius. Fig. 5 compares the two numerical pressures against the analytical result. The pressure peak becomes lower and closer to r=a as we refine the mesh. The finer mesh has pressure in between the coarser mesh and analytical pressures. This suggests that the numerical solution is approaching the analytical one with the mesh refinement. However, due to the linear continuum nature of the code, the peak adjacent to the zero pressure boundary, although becoming lower, would remain for a refined mesh. Another way to improve the agreement is to refine the mesh where the pressure gradient is large, see Appendix C.4.

Table 1
Poroelastic model parameters: Young's modulus E, Poison's ratio ν, fluid mobility k, Biot's coefficient α_B, fluid bulk modulus k_f.

E [Pa]	ν	k [m^2/Pa/s]	α_B	k_f [Pa]
3.0E10	0.25	1.0E-12	0.96	2.2E9

3. Viscoelasticity

For Maxwell power law viscoelasticity, the deformation has affect on the model in both the stiffness matrix $\mathbf{K}_n$ and the RHS function $\Delta\mathbf{F}_n$, Eqs. (4) and (5) by Melosh and Raefsky, 1980.

$$\mathbf{K}_e^{(n+1)} = \int_\Omega \mathbf{B}^T(\mathbf{D}^{-1} + \alpha\Delta t\boldsymbol{\beta}'_n)^{-1}\mathbf{B}d\Omega\mathbf{f}_{n+1} = \int_\Omega \mathbf{B}^T(\mathbf{D}^{-1} + \alpha\Delta t\boldsymbol{\beta}'_n)^{-1}(\Delta t\boldsymbol{\beta}_n)\, d\Omega + \mathbf{F}_{n+1}. \tag{4}$$

where, **B** is displacement to strain matrix depending on the element geometry, Eq. (A.10). **D** is the element stiffness matrix depending on the elastic constants.

$$\boldsymbol{\beta} = \frac{\sigma^{e-1}}{4\eta}\mathbf{C}_c : \boldsymbol{\sigma},\ e \geq 1,\ \sigma = \sqrt{\sum_{i\neq j}(\boldsymbol{\sigma}_{ii} - \boldsymbol{\sigma}_{jj})^2/(2d) + \boldsymbol{\sigma}_{ij}^2},\quad d = 2 \text{ or } 3,$$

$$\mathbf{C}_c = \begin{cases} \begin{bmatrix} 1 & -1 & 0 \\ -1 & 1 & 0 \\ 0 & 0 & 4 \end{bmatrix}, & \text{2D,} \\ \begin{bmatrix} 4/3 & -2/3 & -2/3 & & \\ -2/3 & 4/3 & -2/3 & 0 & \\ 2/3 & -2/3 & 4/3 & & \\ & & & 4 & \\ & 0 & & & 4 \end{bmatrix}, & \text{3D.} \end{cases} \tag{5}$$

$$\boldsymbol{\beta}' = \begin{cases} \frac{\sigma^{e-1}}{4\eta}\begin{bmatrix} c_1 & -c_1 & c_3 \\ -c_1 & c_1 & -c_3 \\ c_3 & -c_3 & 4c_2 \end{bmatrix}, & \text{2D,} \\ \frac{\sigma^{e-1}}{4\eta}\begin{bmatrix} 4/3 + S_x^2 & -2/3 + S_xS_y & -2/3 + S_xS_z & S_xT_1 & S_xT_2 & S_xT_3 \\ -2/3 + S_xS_y & 4/3 + S_y^2 & -2/3 + S_yS_z & S_yT_1 & S_yT_2 & S_yT_3 \\ -2/3 + S_xS_z & -2/3 + S_yS_z & 4/3 + S_z^2 & S_zT_1 & S_zT_2 & S_zT_3 \\ S_xT_1 & S_yT_1 & S_zT_1 & 4 + T_1^2 & T_1T_2 & T_1T_3 \\ S_xT_2 & S_yT_2 & S_zT_2 & T_2T_1 & 4 + T_2^2 & T_2T_3 \\ S_xT_3 & S_yT_3 & S_zT_3 & T_3T_1 & T_3T_2 & 4 + T_3^2 \end{bmatrix}, & \text{3D.} \end{cases}$$

where, e is the viscosity power law parameter. When e=1, η is the linear